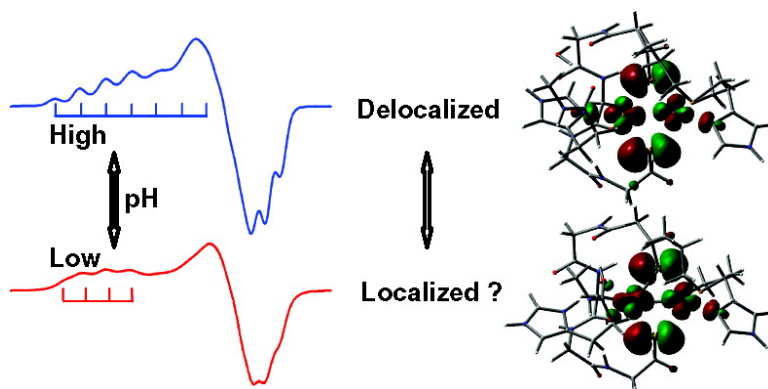Article

Perturbations to the Geometric and Electronic Structure of the Cu Site: Factors that Influence Delocalization and Their Contributions to Electron Transfer

Xiangjin Xie, Serge I. Gorelsky, Ritimukta Sarangi, Dewain K. Garner, Hee Jung Hwang, Keith O. Hodgson, Britt Hedman, Yi Lu, and Edward I. Solomon

More About This Article

Additional resources and features associated with this article are available within the HTML version:

- Supporting Information
- Links to the 1 articles that cite this article, as of the time of this article download
- Access to high resolution figures
- Links to articles and content related to this article
- Copyright permission to reproduce figures and/or text from this article

View the Full Text HTML

Perturbations to the Geometric and Electronic Structure of the Cu$_A$ Site: Factors that Influence Delocalization and Their Contributions to Electron Transfer

Xiangjin Xie,[†] Serge I. Gorelsky,[†] Ritimukta Sarangi,[†] Dewain K. Garner,[§]
Hee Jung Hwang,[§] Keith O. Hodgson,[†,‡] Britt Hedman,[‡] Yi Lu,*,[§] and
Edward I. Solomon*,[†,‡]

*Department of Chemistry, Stanford University, Stanford, California 94305, Department of
Chemistry, University of Illinois at Urbana—Champaign, Urbana, Illinois 61801, and Stanford
Synchrotron Radiation Laboratory, SLAC, Stanford University, Menlo Park, California 94025*

Received November 12, 2007; E-mail: yi-lu@uiuc.edu; edward.solomon@stanford.edu

Abstract: Using a combination of electronic spectroscopies and DFT calculations, the effect of pH perturbation on the geometric and electronic structure of the Cu$_A$ site has been defined. Descriptions are developed for high pH (pH = 7) and low pH (pH = 4) forms of Cu$_A$ azurin and its H120A mutant which address the discrepancies concerning the extent of delocalization indicated by multifrequency EPR and ENDOR data (*J. Am. Chem. Soc.* **2005**, *127*, 7274; *Biophys. J.* **2002**, *82*, 2758). Our resonance Raman and MCD spectra demonstrate that the low pH and H120A mutant forms are essentially identical and are the perturbed forms of the completely delocalized high pH Cu$_A$ site. However, in going from high pH to low pH, a seven-line hyperfine coupling pattern associated with complete delocalization of the electron ($S =$ 1/2) over two Cu coppers ($I_{Cu} = 3/2$) changes into a four-line pattern reflecting apparent localization. DFT calculations show that the unpaired electron is delocalized in the low pH form and reveal that its four-line hyperfine pattern results from the large EPR spectral effects of ∼1% 4s orbital contribution of one Cu to the ground-state spin wave function upon protonative loss of its His ligand. The contribution of the Cu−Cu interaction to electron delocalization in this low symmetry protein site is evaluated, and the possible functional significance of the pH-dependent transition in regulating proton-coupled electron transfer in cytochrome *c* oxidase is discussed.

Introduction

The Cu$_A$ site, found in cytochrome *c* oxidases (C*c*Os),[1–6] nitrous oxide reductases (N$_2$ORs),[7,8] and a nitric oxide reductase (NOR),[9,10] is responsible for rapid intra- and intermolecular electron transfer (ET) in biological systems. C*c*Os catalyze the terminal step of enzymatic aerobic respiration by coupling the four-electron reduction of O$_2$ to H$_2$O to the generation of a proton electrochemical gradient which is the energetic driving force for the synthesis of ATP. NOR reduces two NO to N$_2$O + H$_2$O, and N$_2$OR is the terminal denitrification enzyme

† Department of Chemistry, Stanford University.
§ University of Illinois at Urbana—Champaign.
‡ Stanford Synchrotron Radiation Laboratory, Stanford University.

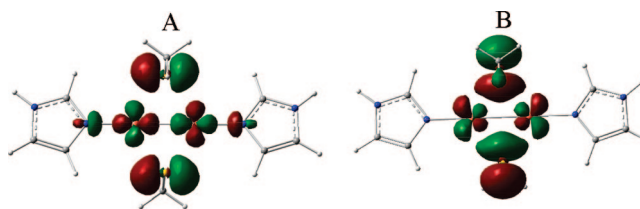(1) Saraste, M. *Q. Rev. Biophys.* **1990**, *23*, 331–366.
(2) Malmström, B. G. *Chem. Rev.* **1990**, *90*, 1247–1260.
(3) Babcock, G. T.; Wikström, M. *Nature* **1992**, *356*, 301–309.
(4) Musser, S. M.; Stowell, M. H. B.; Chan, S. I. *FEBS Lett.* **1993**, *327*, 131–136.
(5) García-Horsman, J. A.; Barquera, B.; Rumbley, J.; Ma, J.; Gennis, R. B. *J. Bacteriol.* **1994**, *176*, 5587–5600.
(6) Wikström, M. *Biochim. Biophys. Acta* **2004**, *1655*, 241.
(7) Kroneck, P. M. H.; Riester, J.; Zumft, W. G.; Antholine, W. E. *Biol. Met.* **1990**, *3*, 103–109.
(8) Zumft, W. G.; Kroneck, P. M. H.; Robert, K. P. *Adv. Microb. Physiol.* **2006**, *52*, 107.
(9) Suharti; Strampraad, M. J. F.; Schroder, I.; de Vries, S. *Biochemistry* **2001**, *40*, 2632–2639.
(10) Suharti; Heering, H. A.; deVries, S. *Biochemistry* **2004**, *43*, 13487–13495.
(11) Tsukihara, T.; Aoyama, H.; Yamashita, E.; Tomizaki, T.; Yamaguchi, H.; Shinzawa-Itoh, K.; Nakashima, R.; Yaono, R.; Yoshikawa, S. *Science* **1995**, *269*, 1069–1074.
(12) Iwata, S.; Ostermeier, C.; Ludig, B.; Michel, H. *Nature* **1995**, *376*, 660–669.
(13) Blackburn, N. J.; Barr, M. E.; Woodruff, W. H.; van der Oost, J.; de Vries, S. *Biochemistry* **1994**, *33*, 10401–10407.
(14) Blackburn, N. J.; de Vries, S.; Barr, M. E.; Houser, R. P.; Tolman, W. B.; Sanders, D.; Fee, J. A. *J. Am. Chem. Soc.* **1997**, *119*, 6135–6143.
(15) Andrew, C. R.; Fraczkiewicz, R.; Czernuszewicz, R. S.; Lappalainen, P.; Saraste, M.; Sanders-Loehr, J. *J. Am. Chem. Soc.* **1996**, *118*, 10436–10445.
(16) Wallace-Williams, S. E.; James, C. A.; de Vries, S.; Saraste, M.; Lappalainen, P.; van der Oost, J.; Fabian, M.; Palmer, G.; Woodruff, W. H. *J. Am. Chem. Soc.* **1996**, *118*, 3986–3987.
(17) Greenwood, C.; Hill, B. C.; Barber, D.; Eglinton, D. G.; Thomson, A. J. *Biochem. J.* **1983**, *215*, 303–316.
(18) Farrar, J. A.; Neese, F.; Lappalainen, P.; Kroneck, P. M. H.; Saraste, M.; Zumft, W. G.; Thomson, A. J. *J. Am. Chem. Soc.* **1996**, *118*, 11501–11514.
(19) Gamelin, D. R.; Randall, D. W.; Hay, M. T.; Houser, R. P.; Mulder, T. C.; Canters, G. W.; de Vries, S.; Tolman, W. B.; Lu, Y.; Solomon, E. I. *J. Am. Chem. Soc.* **1998**, *120*, 5246–5263.
(20) Salgado, J.; Warmerdam, G.; Bubacco, L.; Canters, G. W. *Biochemistry* **1998**, *37*, 7378–7389.
(21) Kroneck, P.; Antholine, W.; Riester, J.; Zumft, W. *FEBS Lett.* **1988**, *242*, 70–74.
(22) von Wachenfeldt, C.; de Vries, S.; van der Oost, J. *FEBS Lett.* **1994**, *340*, 109–113.

reducing N$_2$O to N$_2$ + H$_2$O. In all enzymes, the Cu$_A$ site serves as an ET conduit between an electron source and the catalytic active site.

Previous studies of Cu$_A$ sites in CcOs and N$_2$ORs have defined their geometric and electronic properties through a combination of X-ray crystallography, extended X-ray absorption fine structure (EXAFS), resonance Raman (rR), magnetic circular dichroism (MCD), nuclear magnetic resonance (NMR), electron paramagnetic resonance (EPR), and X-ray absorption spectroscopies (XAS).[11–21] The expression and isolation of engineered and mutant Cu$_A$ sites,[22–27] combined with the successful synthesis of Cu$_A$ model complexes,[28] have strongly facilitated the understanding of the electronic structure of Cu$_A$. The binuclear Cu$_A$ site contains two copper centers bridged by two thiolates, with each copper further coordinated equatorially by one N$_{His}$ and axially by either a S$_{Met}$ or a carbonyl O$_{Glu}$. The Cu$_2$S$_2$ atoms form a diamond core which is nearly planar, with a Cu–Cu distance of 2.40–2.44 Å.[13,14,29,30] In its oxidized state, Cu$_A$ is a completely delocalized (class III[31]) mixed valence Cu$^{1.5+}$–Cu$^{1.5+}$ species.[18,19,21,32,33] The ground-state wave function quantified by XAS is highly covalent with 44% Cu character and 46% S character.[34] This is very similar to the blue copper ground-state wave function; however, in Cu$_A$, the covalency is delocalized over the Cu$_2$S$_2$ dimer. ENDOR studies of Cu$_A$ have shown a total of ~4% spin density over two N$_{His}$ ligands in CcO[35] and ~4% N$_{His}$ character on at least one N$_{His}$ in N$_2$OR.[36] The class III mixed valence $\psi \rightarrow \psi^*$ transition of Cu$_A$ was identified by rR.[16,19] This transition is associated with the valence delocalization of Cu$_A$ providing a measure of the electronic coupling, $2H_{AB}$, between two Cu's. Correlation of the $\psi \rightarrow \psi^*$ transition and Cu/S edge spectroscopies in Cu$_A$ and a model have shown that both direct Cu–Cu and super-exchange through the S bonds contribute to H$_{AB}$. Consistent with those studies, density functional theory (DFT) calculations of the Cu$_A$ site reveal a completely delocalized σ_u^* type ground state (d$_{x^2-y^2}^{Cu1}$ − d$_{x^2-y^2}^{Cu2}$) (Chart 1A), which is the redox active molecular orbital (RAMO). Note that there is also a low-lying

(23) Lappalainen, P.; Aasa, R.; Malmström, B. G.; Saraste, M. *J. Biol. Chem. Rev.* **1993**, *268*, 26416–26421.
(24) Slutter, C. E.; Sanders, D.; Wittung, P.; Malmström, B. G.; Aasa, R.; Richards, J. H.; Gray, H. B.; Fee, J. A. *Biochemistry* **1996**, *36*, 3387–3395.
(25) Zumft, W. G.; Viebrock-Sambale, A.; Braun, C. *Eur. J. Biochem.* **1990**, *192*, 591–599.
(26) Hay, M.; Richards, J.; Lu, Y. *Proc Natl. Acad. Sci. U.S.A.* **1996**, *93*, 461–464.
(27) Dennison, C.; Vijgenboom, E.; de Vries, S.; van der Oost, J.; Canters, G. *FEBS Lett.* **1995**, *365*, 92–94.
(28) Houser, R. P.; Young, V. G., Jr.; Tolman, W. B. *J. Am. Chem. Soc.* **1996**, *118*, 2101–2102.
(29) Tsukihara, T.; Aoyama, H.; Yamashita, E.; Tomizaki, T.; Yamaguchi, H.; Shinzawa-Itoh, K.; Nakashima, R.; Yaono, R.; Yoshikawa, S. *Science* **1996**, *272*, 1136–1144.
(30) Hay, M. T.; Ang, M. C.; Gamelin, D. R.; Solomon, E. I.; Antholine, W. E.; Ralle, M.; Blackburn, N. J.; Massey, P. D.; Wang, X.; Kwon, A. H.; Lu, Y. *Inorg. Chem.* **1998**, *37*, 191–198.
(31) Robin, M. B.; Day, P. *Adv. Inorg. Chem. Radiochem.* **1967**, *10*, 247.
(32) Neese, F.; Zumft, W. G.; Antholine, W. E.; Kroneck, P. M. H. *J. Am. Chem. Soc.* **1996**, *118*, 8692–8699.
(33) Gorelsky, S. I.; Xie, X.; Chen, Y.; Fee, J. A.; Solomon, E. I. *J. Am. Chem. Soc.* **2006**, *128*, 16452–16453.
(34) George, S. D.; Metz, M.; Szilagyi, R. K.; Wang, H.; Cramer, S. P.; Lu, Y.; Tolman, W. B.; Hedman, B.; Hodgson, K. O.; Solomon, E. I. *J. Am. Chem. Soc.* **2001**, *123*, 5757–5767.
(35) Gurbiel, R. J.; Fann, Y. C.; Surerus, K. K.; Werst, M. M.; Musser, S. M.; Doan, P. E.; Chan, S. I.; Fee, J. A.; Hoffman, B. M. *J. Am. Chem. Soc.* **1993**, *115*, 10888–10894.
(36) Neese, F.; Kappl, R.; Hüttermann, J.; Zumft, W. G.; Kroneck, P. M. H. *J. Biol. Inorg. Chem.* **1998**, *3*, 53–67.

Chart 1

π_u exited state (d$_{xy}^{Cu1}$ + d$_{xy}^{Cu2}$) (Chart 1B), responsible for various spectroscopic features (vide infra).

Engineered Cu$_A$ azurin exhibits a very interesting pH effect.[37] It displays a mixed valence EPR spectrum with a seven-line hyperfine pattern associated with the delocalization of the $S = 1/2$ over two Cu centers ($I_{Cu} = 3/2$). Upon lowering the pH to 4.0, the EPR hyperfine coupling changed to a four-line pattern, indicating apparent spin localization. This pH-dependent transition is reversible with a pK_a value of ~5. It has been suggested that this change in EPR signal can be related to a perturbation of the H120 ligand, which has an imidazole nitrogen equatorially coordinated to the Cu with an axial carbonyl O$_{Glu}$ ligand. The H120 ligand is located near the protein surface and could be protonated at low pH. Interestingly, the H120A mutant has very similar spectral features to the low-pH form, and the pH-dependent transition is eliminated. Multifrequency EPR data have indicated that the electron spin in the H120A mutant is localized based on a four-line Cu hyperfine pattern.[38] However, ENDOR data indicate that the site is delocalized based on superhyperfine couplings of cysteine C$_\beta$ protons and histidine nitrogens.[38]

In this study, we address this apparent discrepancy through a series of electronic spectroscopic studies of the high-pH and low-pH forms of Cu$_A$ azurin and its H120A mutant combined with DFT calculations. Our studies define the geometric and electronic structure of the low-pH form of Cu$_A$ azurin and its H120A mutant, elucidate the extent of electron delocalization and the contribution of the low-lying π_u excited-state to the ground-state spectral features, and provide further insight into the factors contributing to delocalization (and the associated facile ET of Cu$_A$) in the low-symmetry protein environment. The possible contribution of the pH-dependent transition to proton-coupled electron transfer (PCET) in CcO is discussed.

Experiments

A. Sample Preparation. The Cu$_A$ construct engineered into *Pseudomonas aeruginosa* azurin[26] and its mutant H120A[39] were prepared as described previously.

B. Electron Paramagnetic Resonance. EPR spectra were obtained using a Bruker EMX spectrometer, an ER 041 XG microwave bridge, and an ER 4102ST cavity. All X-band samples were run at 77 K in a liquid nitrogen finger Dewar. A Cu standard (1.0 mM CuSO$_4$·5H$_2$O with 1 mM HCl and 2 M Na$_2$ClO$_4$) was used for spin quantitation of the EPR spectra. All Q-band spectra were obtained at 77 K using an ER 051 QR microwave bridge, an ER 5106QT resonator, and an Oxford continuous-flow CF935 cryostat. EPR spectra were baseline-corrected and simulated using XSophe (Bruker). For each protein, X- and Q-band spectra were simultaneously fit in order to constrain the simulation parameters

(37) Hwang, H. J.; Lu, L. *Proc. Natl. Acad. Sci. U.S.A.* **2004**, *101*, 12842–12847.
(38) Lukoyanov, D.; Berry, S. M.; Lu, Y.; Antholine, W. E.; Scholes, C. P. *Biophys. J.* **2002**, *82*, 2758–2766.
(39) Wang, X.; Berry, S. M.; Xia, Y.; Lu, Y. *J. Am. Chem. Soc.* **1999**, *121*, 7449–7450.

(*g* values were obtained from Q-band data and hyperfine coupling from X-band data).

C. Electronic Absorption and MCD Spectroscopies. Low-temperature absorption data were collected on a Cary-17 spectrometer using a Janis Research Super Vari-Temp cryogenic Dewar mounted in the optical path. MCD measurements were performed on Jasco J810 (UV/vis, S1 and S20 PMT detection) and J200 (NIR, liquid N_2-cooled InSb detection) spectropolarimeters equipped with an Oxford Instruments SM4000-7 T (*T*) superconducting magnet/cryostats. The MCD spectra were corrected for the natural CD and zero-field baseline effects caused by the strain in glass by averaging the positive and negative field data at 5 K ([7*T* − (−)7*T*]/2). Samples of ~1 mM Cu_A-containing protein in NH_4OAc buffer (pH = 4 and 7 for wt Cu_A azurin, pH = 5 for the H120A mutant) were diluted with glycerol-d_3 (~50% v/v) and injected into sample cells composed of two quartz disks separated by a Viton O-ring spacer. The concentrations of the protein were determined by EPR spin quantitation.

D. Resonance Raman Spectroscopy. The rR spectra were obtained using continuous wave (CW) excitation from Kr^+ (Coherent I90K) and Ar^+ (Coherent I18UV and CR18) ion laser sources. A Ti-sapphire (Coherent 890) laser was used for the NIR region. Incident power in the range of ~25 mW was used in a ~135° backscattering arrangement. Spectra were measured using a SPEX model 1877 CP triple monochromator with 1200, 1800, and 2400 grooves/mm holographic gratings, equipped with a Princeton Instruments back-illuminated CCD detector. The resolution was 2 cm^{-1} at all excitation energies. Solution samples were frozen in NMR tubes placed in a liquid nitrogen finger Dewar. Excitation profile intensities of Raman scattering peaks were determined relative to the 230 cm^{-1} ice peak in protein samples.

E. XAS Data Acquisition. The X-ray absorption spectra were measured at the Stanford Synchrotron Radiation Laboratory on the focused 16-pole 2.0 T wiggler beam line 9-3 under standard ring conditions of 3 GeV and 80–100 mA. A Si(220) double crystal monochromator was used for energy selection. A Rh-coated harmonic rejection mirror and a cylindrical Rh-coated bent focusing mirror were used on beam line 9-3 to reject components of higher harmonics. During data collection, the samples were maintained at a constant temperature of 10 K using an Oxford Instruments CF 1208 liquid helium cryostat. Fluorescence mode was used to measure data to $k = 13.4$ Å^{-1} employing a Canberra Ge 30-element solid array detector. Internal energy calibration was accomplished by simultaneous measurement of the absorption of a Cu foil placed between two ionization chambers situated after the sample. The first inflection point of the foil spectrum was set at 8980.3 eV. Data presented here are 13-scan (wt, pH 6), 8-scan (wt, pH 4), and 9-scan (H120A, pH 6) averaged spectra, which were processed by fitting a second-order polynomial to the pre-edge region and subtracting this from the entire spectrum as background. A three-region spline of orders 2, 3, and 3 was used to model the smoothly decaying postedge region. The data were normalized by subtracting the cubic spline and assigning the edge jump to 1.0 at 9000 eV using the PySpline program.[40] The crystal structure of Cu_A azurin (PDB code 1CC3) was used to calculate the theoretical EXAFS phase and amplitude parameters using FEFF (version 7.0)[41,42] and fit to the data using EXAFSPAK.[43] The structural parameters allowed to vary during the fitting process were the bond length (*R*) and the bond variance (σ^2), which is related to the Debye–Waller factor resulting from thermal motion and static disorder. The nonstructural parameter E_0 (the energy at which $k = 0$) was also allowed to vary but

was restricted to a common value for every component in a given fit. Coordination numbers were systematically varied in the course of the fit but were fixed within a given fit.

For the Cu K-edge experiments, the protein concentrations (in Cu content) were ~2.5 mM for wt and ~5 mM for H120A mutant. The samples were prepared in NH_4OAc buffer. Thirty percent glycerol was added to the protein solution as a glassing agent. Samples were loaded into Lucite XAS cell holders and inserted into 2 mm Lucite XAS cells with 63.5 μm Mylar windows. All samples were rapidly frozen by immersion in liquid N_2 and kept at or below this temperature.

F. DFT Calculations. A 96-atom model (47 heavy atoms) was used to match the high-pH Cu_A site. A partial geometry optimization was performed, where positions of the protein backbone carbon, nitrogen, and oxygen atoms were frozen to those in the 1.65 Å resolution X-ray structure of the engineered Cu_A azurin (PDB ID: 1CC3). In order to model the pH effect on the Cu_A site, additional calculations were performed, with ligand H120 protonated (97 atoms). DFT calculations were performed using the program Gaussian 03.[44] Spin-unrestricted DFT was employed to model the open-shell species. Optimized molecular geometries were calculated using the hybrid B3LYP exchange-correlation functional[45–47] with tight SCF convergence criteria (10^{-8} au) and the mixed triple-ζ/double-ζ (TZVP on Cu and S and 6-31G* on the other atoms) basis sets. Wave function stability calculations were performed to confirm the calculated wave functions corresponded to the ground state. Time-dependent DFT (TD-DFT) was used to calculate the energies and intensities of the 30 lowest-energy, spin-allowed electronic transitions. The calculated absorption energies and intensities were transformed with the SWizard program[48] into simulated spectra, using Gaussian with half-widths of 2600 cm^{-1}.

EPR hyperfine coupling parameters were calculated on the above geometry optimized models using the program ORCA.[49] This employed the hybrid functional B3LYP with the CoreProp basis set[50] for Cu and the SVP basis set[51] for other atoms. These bases are the TurboMole DZ bases developed by Ahlrichs and co-workers and obtained from the basis set library.[52]

Results and Analysis

I. Spectroscopy. A. Electron Paramagnetic Resonance. Figure 1 shows the X- and Q-band EPR spectra of the high-pH (at pH = 7) and the low-pH (at pH = 4) forms of wt Cu_A−azurin protein and the H120A mutant. Table 1 gives the $g_{\parallel}$ values and hyperfine coupling parameters obtained by XSophe simulation of the X-band data. The *g* values were extracted from the Q-band data and then correlated to X-band spectra.

At high pH, Cu_A azurin has a $g_{\parallel}$ value of 2.173 and a $g_{\perp}$ value of 2.022 (Figure 1, black, Table 1). At low pH, Cu_A azurin has $g_{\parallel} = 2.222$ and $g_{\perp} = 2.010$ (Figure 1, red, Table 1), which are similar to the *g* values for the H120A mutant (Figure 1, green, Table 1). The g_x−g_y anisotropy was <0.01 in all cases. The $g_{\parallel} > g_{\perp} > 2.0023$ pattern indicates that all these forms of Cu_A have a $d_{x^2−y^2}$ ground state, where the electron can be delocalized over two coppers.

(40) Tenderholt, A. 2005, *PySpline*, Stanford University, Stanford, CA 94305.

(41) Muestre de Leon, J.; Rehr, J. J.; Zabinsky, S. I.; Albers, R. C. *Phys. Rev. B* **1991**, *44*, 4146–4156.

(42) Rehr, J. J.; Muestre de Leon, J.; Zabinsky, S. I.; Albers, R. C. *J. Am. Chem. Soc.* **1991**, *113*, 5135–5140.

(43) George, G. N. *EXAFSPAK & EDG_FIT, Stanford Synchrotron Radiation Laboratory, Stanford Linear Accelerator Center*, Stanford University, Stanford, CA 94309, 2000.
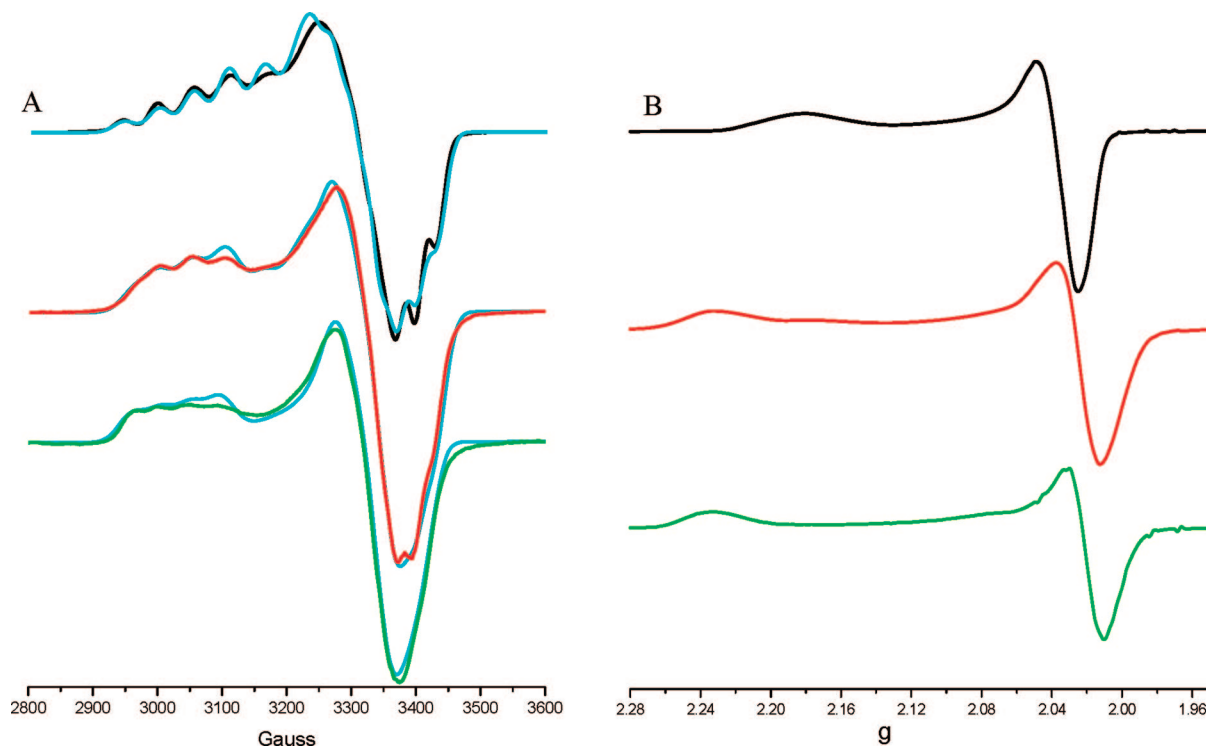
(44) Frisch, M. J.; *Gaussian 03*, revision C.02; Gaussian, Inc.: Wallingford, CT, 2004.

(45) Perdew, J. P. *Phys. Rev. B* **1986**, *33*, 8822.

(46) Becke, A. D. *Phys. Rev. A* **1988**, *38*, 3098.

(47) Becke, A. D. *J. Chem. Phys.* **1993**, *98*, 5648.

(48) Gorelsky, S. I. *SWizard*; Department of Chemistry, York University: Toronto, ON, 1999; http://www.sg-chem.net.

(49) Neese, F. ORCA, version 2.5; Universität Bonn: Bonn, Germany. The program is available free of charge at http://www.thch.uni-bonn.de/tc/orca.

(50) Neese, F. *Inorg. Chim. Acta* **2002**, *337*, 181–192.

(51) Schäfer, A.; Horn, H.; Ahlrichs, R. *J. Chem. Phys.* **1992**, *97*, 2571–2577.

(52) See: ftp.chemie.unikarlsruhe.de/pub/basen.

Figure 1. (A) X-band EPR spectra. Microwave frequency, 9.46 GHz; temperature 77 K. (B) Q-band EPR spectra. Microwave frequency, 33.86 GHz; temperature 77 K; the high-pH form (black), the low-pH form (red), the H120A mutant (green), and XSophe simulations (blue).

Table 1. EPR Parameters of the High- and Low-pH Forms of Cu$_A$ Azurin and Its H120A Mutant

	g_x	g_y	g_z	A_x^{Cu1}, A_x^{Cu2} $(10^{-4}$ cm$^{-1})$	A_y^{Cu1}, A_y^{Cu2} $(10^{-4}$ cm$^{-1})$	A_z^{Cu1}, A_z^{Cu2} $(10^{-4}$ cm$^{-1})$
high-pH form	2.022	2.022	2.173	25, 27	25, 26	53, 53
low-pH form[a]	2.010	2.010	2.222	26, 21	21, 24	43, 12
H120A	2.010	2.010	2.225	24, 19	19, 24	46, 7

[a] Note that the low-pH form still has ~10% of the high-pH form as the pk_a is ~5. This is included in EPR spectral simulation.

At high pH, Cu$_A$ azurin displays a seven-line hyperfine coupling pattern in the $g_{||}$ region. The seven hyperfine lines are associated with complete delocalization of the unpaired electron ($S = 1/2$) over two equivalent coppers, each with $I = 3/2$. Consistent with this, XSophe simulations (Table 1) show that this high-pH form has equivalent hyperfine coupling of the two coppers: $A_{||}^{Cu_1} = A_{||}^{Cu_2} = |53| \times 10^{-4}$ cm^{-1} and $A_\perp^{Cu_1} = A_\perp^{Cu_2} = |26| \times 10^{-4}$ cm^{-1}.

Upon going to low pH, the EPR spectrum goes to a four-line hyperfine coupling pattern in the $g_{||}$ region, indicating that there is a large inequivalence in the hyperfine coupling of each Cu nucleus to the $S = 1/2$, and the unpaired electron appears to be localized. In Table 1, the XSophe simulations give $A_{||}^{Cu_1} = |43| \times 10^{-4}$ cm^{-1}, $A_{||}^{Cu_2} = |12| \times 10^{-4}$ cm^{-1}, and $A_\perp^{Cu_1}$ and Cu$_2$ in the range between $|21| \times 10^{-4}$ and $|26| \times 10^{-4}$ cm^{-1}.

The EPR spectra of the H120A mutant are equivalent to those of the low-pH form (Figure 1, green, Table 1). The similarities in these spectra indicate that the ground-state wave functions of the copper centers in the two proteins are very similar. The pH effect is eliminated in the H120A mutant; thus for the low-pH case, the His ligand (H120) becomes protonated, and this changes the EPR signal such that the hyperfine coupling of the electron spin to one Cu is greatly decreased.

B. Electronic Absorption and MCD Spectroscopy. A comparison of the low-temperature Abs and MCD spectra of the high-pH and low-pH forms and the H120A mutant is shown in Figure 2. (In Supporting Information (Figure S1), LT Abs and MCD peaks are simultaneously fit and correlated to the peaks in the room temperature CD spectrum).

Simulations of the Abs and MCD spectra identify a series of seven electronic transitions in the range from 8000 to 22 000 cm^{-1}. The high-pH form has two peaks (band 6 and 7) in the Abs spectrum between 18 000 and 22 000 cm^{-1} and an associated intense derivative-shaped pseudo-A term in the low-temperature MCD spectrum, which have been assigned as the S$_{cys}$ → Cu charge transfer (CT) transitions by rR.[19] Band 2 at 13 300 cm^{-1}, which is relatively intense in Abs, exhibits a negative C-term MCD signal and has been assigned by rR studies as the $\psi \rightarrow \psi^*$ transition. This involves excitation of an electron from the σ_g Cu–Cu bonding (d$_{x^2-y^2}^{Cu1}$ + d$_{x^2-y^2}^{Cu2}$) orbital to the σ_u antibonding (d$_{x^2-y^2}^{Cu1}$ – d$_{x^2-y^2}^{Cu2}$) orbital and reflects a class III mixed valence system.[19]

From Figure 2, the Abs and MCD spectra of the low-pH and mutant forms are equivalent. Both are dominated by three intense absorption features at ~19 000 (band 6), ~20 400 (band 7), and ~12 200 cm^{-1} (band 2), with several additional weaker features also observed at lower and higher energies. These are also very similar to the Abs and MCD spectra of the high-pH form, but with an 1100 cm^{-1} shift of band 2 to lower energy both in Abs and in MCD. The similarity among the spectra in Figure 2 confirms that the low-pH form and the H120A mutant are essentially identical and can be treated as perturbations of the high-pH form.

C. Resonance Raman Spectroscopy. Figure 3 shows the rR spectra obtained for the three proteins (rR excitation profiles are shown in Figure S2 in Supporting Information). The rR spectra of the high-pH form are similar to those previously reported for the Cu$_A$ site but are clarified by going to a high enough pH to eliminate low pH contributions. Excitation into
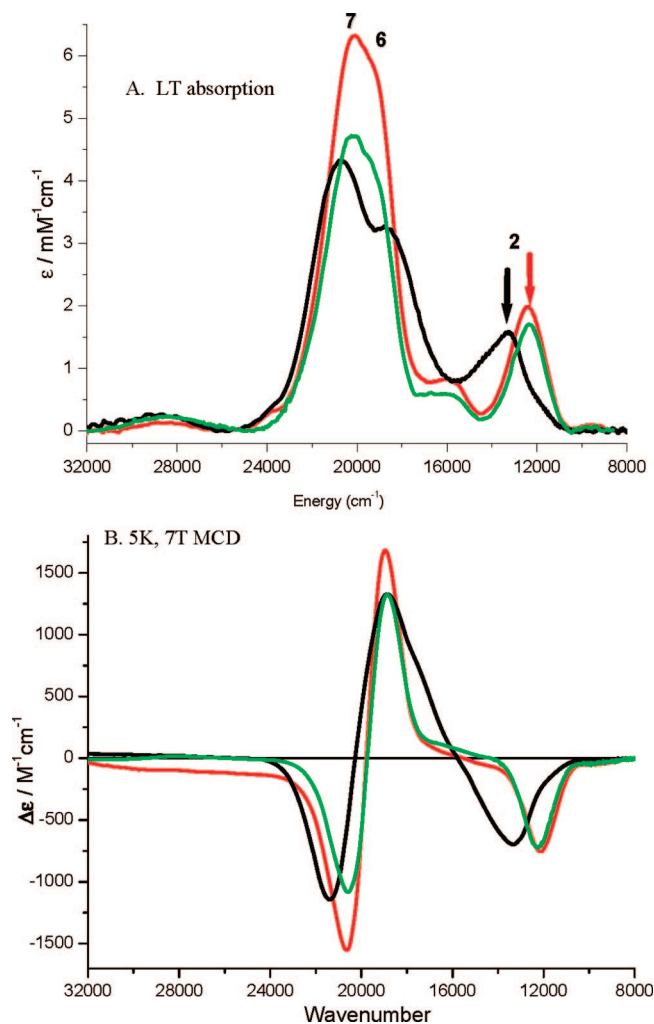
Figure 2. Low-temperature absorption and MCD spectra of the high-pH form (black), the low-pH form (red), and the H120A mutant (green).

the $S_{Cys} \rightarrow$ Cu CT transition at 477 nm produces strong resonance enhancement of the symmetric breathing mode at 337 cm^{-1} (ν_4), an out-of-phase "twisting" Cu–S stretching modes at 274 cm^{-1} (ν_3), and a mixed Cu–S/Cu–N stretching mode at 256 cm^{-1} (ν_2), as described previously[15] and illustrated in Chart 2. There is essentially no resonance enhancement of the Cu$_2$S$_2$ "accordion" mode (ν_1, in Chart 2). However, excitation into absorption band 2 at 750 nm for the high-pH form shows a dramatically different intensity distribution: the intensities of ν_2 and ν_3 vibrations dramatically decrease, and that of the ν_1 accordion mode at 158 cm^{-1}[53] gains significant resonance enhancement relative to the 337 cm^{-1} (ν_4) breathing mode. Thus excitation into band 2 activates the distortions of the Cu$_2$S$_2$ site along the ν_1 and ν_4 modes in the associated excited state, resulting in a large elongation of the Cu–Cu bond with little change in Cu–S$_{Cys}$ and Cu–N$_{His}$ bond lengths. Band 2 was assigned as the $\psi \rightarrow \psi^*$ transition since only totally symmetric vibrations of the Cu$_2$S$_2$ core are observed.[16,19] The rR data are consistent with the valence delocalized ground state of Cu$_A$.

For the low-pH and H120A mutant forms, excitation into band 2 also gives a dramatic enhancement of the ν_1 and ν_4 modes with $\nu_2 + \nu_3$ greatly decreased; therefore, band 2 in the

low-pH and H120A mutant forms can also be assigned as the $\psi \rightarrow \psi^*$ transition, indicating an equivalent excited-state distortion to that observed in the high-pH form. On the basis of these excited-state data, the low-pH and H120A mutant forms of Cu$_A$ are still delocalized. The ν_1 goes up by 10 cm^{-1}, indicating a stronger Cu–Cu bonding interaction.

Further, rR excitation into the $S_{Cys} \rightarrow$ Cu CT region in the low-pH and mutant forms shows that one of the two Cu–N$_{His}$ vibrations contributing to ν_2 at ~256 cm^{-1} in the high-pH form is eliminated. This indicates that upon going to the low-pH form, one histidine ligand is lost, as is also, of course, the case for the H120A mutant which exhibits the equivalent rR spectrum as the low-pH form.

D. EXAFS Studies. Figure 4A shows a comparison of the Cu K-edge EXAFS and the corresponding nonphase shift corrected Fourier transform data for the high-pH and the low-pH forms of Cu$_A$ and the H120A mutant. Figures S3, S4, and S5 show the fits to these EXAFS data. EXAFS fit parameters are summarized in Table 2. The first shell of the high-pH site was fit with one Cu–N contribution at 1.92 Å, two Cu–S contributions at 2.27 Å, and one Cu–Cu contribution at 2.40 Å.[54] The first shell of the low-pH site was fit with a 0.5 Cu–N contribution at 1.95 Å, two Cu–S contributions at 2.26 Å, and one Cu–Cu contribution at 2.36 Å. The first shell of H120A Cu$_A$ was fit with a 0.5 Cu–N contribution at 1.93 Å, two Cu–S contributions at 2.26 Å, and one Cu–Cu contribution at 2.36 Å. Second and third shells of the data for all three proteins were fit to the single and multiple scattering contributions from the histidine ring(s).

The EXAFS fits indicate that the two Cu–S contributions (~2.27 Å) due to the two Cu–S$_{Cys}$ bonds remain very similar in the three sites. Interestingly, however, the EXAFS fits show that the low-pH and H120A mutant data have only 0.5 Cu–N contribution to the first shell, indicating that one of the Cu–N$_{His}$ ligands is lost at low pH and in the His to Ala mutation. Note that DFT calculations (vide infra) indicate that the Cu–O$_{Glu}$ becomes shorter for these two forms (~2.1 Å) and a weak Cu–O$_{H_2O}$ bond (2.26 Å) replaces the Cu–N$_{His}$ bond (Table 3). Attempts to fit the EXAFS data with a 0.5 Cu–O component at 2.1 and 2.26 Å were unsuccessful, indicating that, if present, the Cu–O bond does not significantly contribute to the EXAFS spectrum. This is consistent with the rR data which indicate that one Cu–N$_{His}$ ligand is lost at low pH and in the His to Ala mutation. Although the first shell Cu–N component indicates the loss of one Cu–N$_{His}$ ligand, a similar decrease in the second and third shell contribution is not observed (see Supporting Information). This likely results from the decreased Cu–O$_{Glu}$ bond distance and associated increase in the multiple-scattering contribution from the carbon atoms of the glutamic acid ligand which can compensate for the loss of the Cu–N$_{His}$ ligand.

The EXAFS data for the low-pH sample and the H120A mutant overlap over the entire k range. A significant difference in the range of k = 8–13 Å^{-1} is observed between the EXAFS data for the high-pH and low-pH forms. The shift in the EXAFS beat-pattern to higher k in the low-pH form and the H120A mutant is a clear indication of a change in the Cu–Cu distance,

(53) This is increased from the 130 cm^{-1} of past studies on *B.s.* CuA due to a shorter Cu–Cu bond in CuA azurin.

(54) The Cu K-edge EXAFS data of wt Cu$_A$ azurin at pH 5.1 has been previously reported in ref 30. The pH titrations on wt CuA azurin show a pK_a value of ~5 for the two different pH-dependent electronic structures observed from UV–vis and EPR data. Thus, the reported EXAFS spectrum represents an approximately equal mixture of the two forms and hence quantitatively differs from the high pH spectrum presented here.
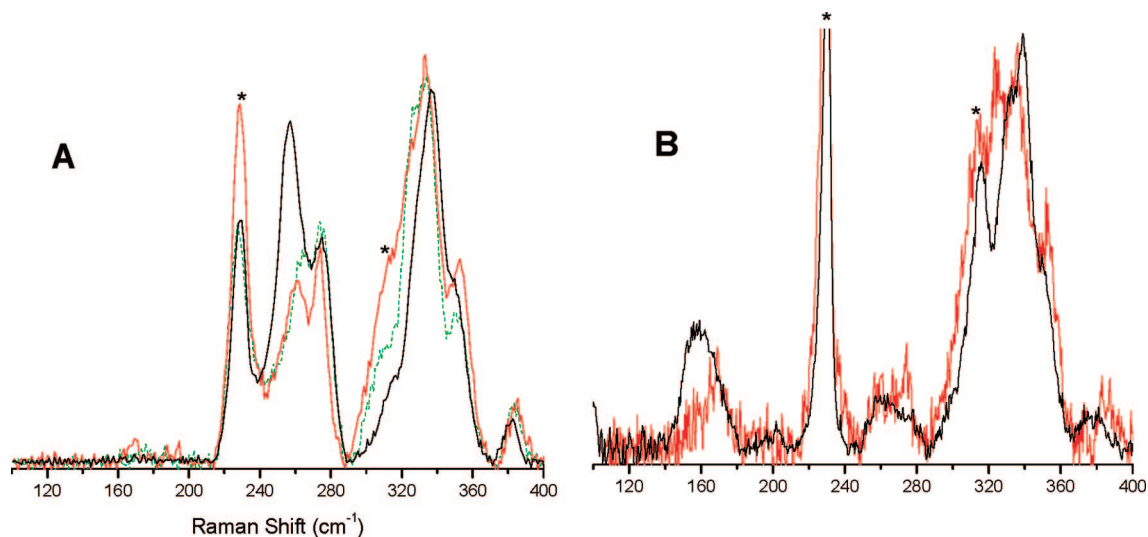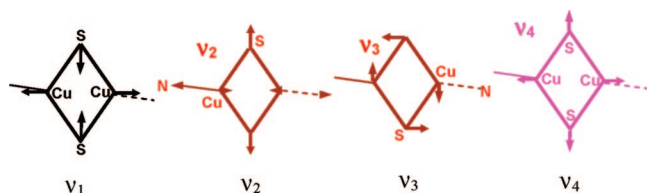
Figure 3. Resonance Raman spectra of (A) S $\rightarrow$ Cu CT band exitation and (B) $\psi \rightarrow \psi^*$ band excitation (high pH form, black; low pH form, red; and H120A mutant, green; solvent peaks are marked with stars).

Chart 2

which has the maximum contribution to the EXAFS data in the high k region. Indeed, EXAFS fits show that the Cu−Cu component in the EXAFS data for the low-pH sample and H120A mutant (2.36 Å) is shorter relative to that in the high-pH form (2.40 Å) (Table 1). This is consistent with the rR data showing an increase in the frequency of ν_1, which indicates an increase in the Cu−Cu bond strength.
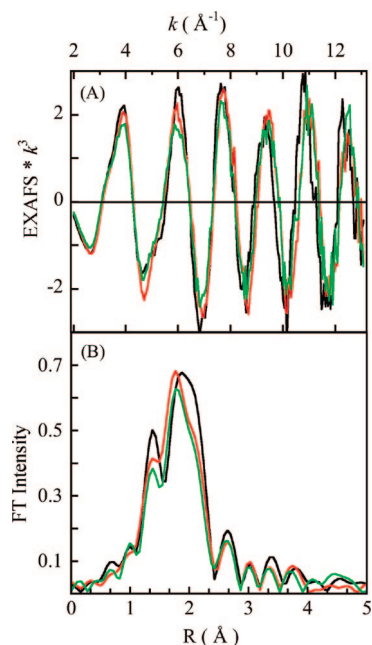

Figure 4. (A) EXAFS data and (B) the corresponding nonphase shift corrected Fourier transforms of wt Cu$_A$ azurin at high pH (black), low pH (red), and the H120A mutant (green).

Table 2. EXAFS Least Squares Fitting Results for Wild Type Cu$_A$ at High pH and Low pH and for the H120A Mutant

	coord/Path	R (Å)^a	σ^2(Å^2)^b	E_0 (eV)	F^c
high-pH form	1 Cu−N/O	1.92	343	−14.7	0.10
	2 Cu−S	2.27	740		
	1 Cu−Cu	2.40	635		
low-pH form	1 Cu−N/O	1.95	343	−12.6	0.05
	2 Cu−S	2.26	614		
	1 Cu−Cu	2.36	668		
H120A	1 Cu−N/O	1.92	389	−14.3	0.06
	2 Cu−S	2.26	648		
	1 Cu−Cu	2.36	689		

^{a} The estimated standard deviations for the distances are in the order of ± 0.02 Å (for the first shell). ^{b} The σ^2 values are multiplied by 10^5. The σ^2 factor of the multiple scattering path is linked to that of the corresponding single scattering path. ^{c} Error is given by $\Sigma[(\chi_{\text{obsd}} - \chi_{\text{calcd}})^2 k^6]/\Sigma[(\chi_{\text{obsd}})^2 k^6]$.

Table 3. The Bond Distances in the X-ray Crystal Structure of Cu$_A$ Azurin, DFT Geometry Optimized 96-Atom and 97-Atom Models

	96-atom model	97-atom model	Cu$_A$ azurin crystal structure	
			A	B
S1−Cu$_O$	2.38	2.31	2.30	2.33
S1−Cu$_S$	2.34	2.41	2.29	2.44
S3−Cu$_S$	2.36	2.40	2.42	2.30
S3−Cu$_O$	2.34	2.33	2.46	3.43
Cu−Cu	2.50	2.46	2.42	2.35
Cu$_O$−N$_{\text{His}}$/O$_{\text{H}_2\text{O}}$	2.02	2.26	2.06	2.26
Cu$_S$−N$_{\text{His}}$	2.04	2.03	2.01	2.08
S$_{\text{Met}}$−Cu$_S$	2.79	2.64	2.98	3.16
Cu$_O$−O$_{\text{Glu}}$	2.34	2.08	2.17	2.15

II. DFT Calculations. A. Optimized Structures. DFT calculations were used to evaluate the change in geometric and electronic structure of the Cu$_A$ site associated with the protonation of one histidine ligand.

In the geometry optimized 96-atom model of the high-pH site (Figure 5A and Table 3), the Cu$_2$S$_2$ core is very symmetric with the Cu−S$_{\text{Cys}}$ distances of 2.34−2.38 Å and a Cu−Cu distance of 2.50 Å. The equatorial Cu−N$_{\text{His}}$ distances are both 2.03 Å. The axial Cu−S$_{\text{Met}}$ distance is calculated to be 2.79 Å, and the Cu−O$_{\text{Glu}}$ distance obtained is 2.34 Å.

Upon protonation of the His120 ligand on Cu$_O$ (97-atom model, Figure 5B, the labels Cu$_S$ and Cu$_O$ denote the copper
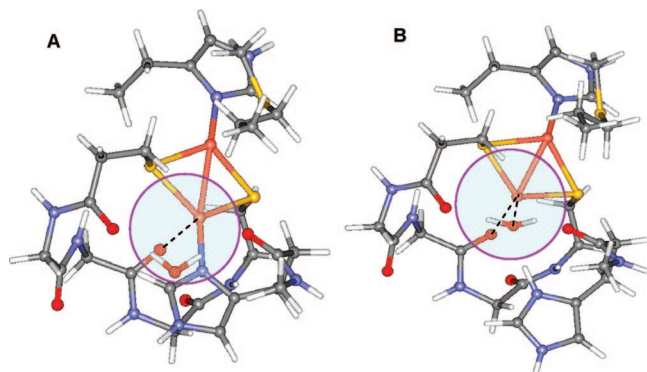
Figure 5. DFT geometry optimized structures of (A) 96-atom model of the high-pH form; (B) 97-atom model of the low-pH form/H120 mutant.

with a weak axial methionine sulfur and carbonyl oxygen ligand, respectively), this His comes off and is replaced by a nearby H_2O ligand with a $Cu_O-O_{H_2O}$ distance of 2.26 Å, and the $Cu-O_{Glu}$ distance is decreased to 2.08 Å. The Cu_2S_2 core is also perturbed with the $Cu-S_{Cys}$ distances of 2.31−2.40 Å. The $Cu-Cu$ distance is decreased to 2.46 Å, and the remaining Cu_S-N_{His} distance is not changed.

The trends of bond length changes from the 96-atom model to the 97-atom model are consistent with the crystal structure data and EXAFS results of the Cu_A site. From the crystal structure of Cu_A azurin,[55] two slightly different Cu_A sites, A and B in the asymmetric unit, were observed (Table 3). In both sites, the average $Cu-S$ distances are similar (2.37 and 2.38 Å, respectively), and the Cu_S-N_{His} distances are also very close (2.01 and 2.08 Å, respectively). However, for the B site relative to the A site, the $Cu-Cu$ distance slightly decreased (2.42 to 2.35 Å), and the $Cu-N_{His}$ distance at the Cu_O sites differs by 0.2 Å (2.06 and 2.26 Å). Since the protein was crystallized at pH = 5, near the pK_a of coordinated H120, it is possible that the two forms of Cu_A sites resolved in the crystal structure are related to the high-pH and low-pH forms, although they can simply reflect independent refinements to disordered structures. The EXAFS data also reveal similar structural differences between the high-pH and low-pH forms (vide supra). In particular, the $Cu-Cu$ distance of the high-pH form is 0.04 Å longer than that of the low-pH form, and only 0.5 $Cu-N_{His}$ contribution with a distance of 1.92 Å was found in the low-pH form. Thus, the 96-atom and 97-atom models reasonably reproduce the high-pH and low-pH forms, respectively, of Cu_A.

B. Ground-State Electronic Structure. (i) Ground-State Wave Function. In the high-pH Cu_A model, the DFT calculations give a σ_u^* ground state with a total of 48% electron spin (Mulliken population analysis) approximately equivalently delocalized over the two coppers, 44% electron spin over the two bridging S_{Cys}'s, and a total of 7% electron spin over the two N_{His}'s (Figure 6A, Table 4). This spin density distribution is close to the experimental results (44% Cu character and 46% S character in the ground-state wave function).[34] For the Cu's, the electron spin is mostly in 3d orbitals (Table 5).

In the low-pH model, the water ligand substitution of His120 produces a distorted ligand field on Cu_O (Figure 5B). However, the σ_u^* ground-state wave function of the low-pH form still shows about the same electron spin delocalization over the two Cu's, two S's, and the remaining N (Figure 6B, Table 4). Both
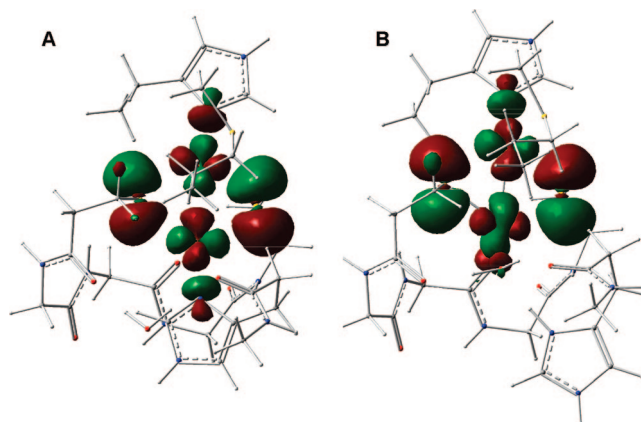
(55) Robinson, H.; Ang, M. C.; Gao, Y.-G.; Hay, M. T.; Lu, Y.; Wang, A. H.-J. *Biochemistry* **1999**, *38*, 5677–5683.

Figure 6. β-LUMOs with the contour values of 0.03 au: (A) 96-atom model of the high-pH form; (B) 97-atom model of the low-pH form.

Table 4. Mulliken Atomic Spin Densities of 96-Atom and 97-Atom Models from Gaussian 03 Calculations

	Cu_O	Cu_S	S_1	S_2	N_O/O	N_S
96-atom model	26	22	19	25	4	3
97-atom model	24	25	21	23	1	4

Table 5. Löwdin Population Analyses of Cu Characters in β-LUMO of 96-Atom and 97-Atom Models from Orca 2.5 Calculations

		β-LUMO								
		s	p_z	p_x	p1	d_{z^2}	d_{xz}	d_{yz}	d_{x-y^2}	d_{xy}	d_{total}^a
96-atom model	Cu_O	0.1	0.2	0.2	0.0	0.2	1.0	0.0	28.6	0.1	29.9
	Cu_S	0.1	0.0	0.2	0.1	0.1	0.5	0.0	24.0	1.3	25.9
97-atom model	Cu_O	1.1	0.0	0.0	0.0	2.1	0.5	0.2	23.7	0.1	26.6
	Cu_S	0.0	0.1	0.2	0.0	0.8	2.5	0.0	25.7	0.3	29.3

^{a} The Cu characters are slightly different from those in Table 4 because a different program, Orca, with a different population analysis (Löwdin) was employed (hyperfine coupling calculations were also done in program Orca).

the high-pH and low-pH forms are calculated to be valence delocalized, which corroborates the correlation of the rR and Abs/MCD spectra. The electron spin on both centers is dominantly in $3d_{x^2-y^2}$ orbitals consistent with the EPR g values (vide supra). However, the spin density distribution of the low-pH form has a limited but important difference relative to the high-pH model. From Table 5, the distorted ligand field produces ~1% Cu_O 4s mixing into the ground-state wave function of the binuclear site. As evaluated below, this ~1% 4s mixing dramatically changes the Fermi contact contribution to the hyperfine coupling for Cu_O in the binuclear Cu center.

(ii) Cu Hyperfine Coupling. These calculations have been performed with the program ORCA 2.5. There are three terms contributing to the hyperfine coupling of the electron spin to the nuclear spin on the Cu: Fermi contact (FC), spin dipolar (SD), and orbital dipolar (OD).

From Table 6, the FC contributions to Cu_S in both high-pH and low-pH models are very similar, $A_{high-pH}^{Cu_S}$ form (FC) = −53 × 10^{-4} cm^{-1}, $A_{low-pH}^{Cu_S}$ form (FC) = −56 × 10^{-4} cm^{-1}, respectively. However, this contribution to Cu_O has changed dramatically from −58 × 10^{-4} cm^{-1} in the high-pH model to −20 × 10^{-4} cm^{-1} in the low-pH model. The SD contributions to Cu_S for the two models are also very similar. In the low-pH form, this term for Cu_O decreases $A_{||}$ by 15 × 10^{-4} cm^{-1} and results in a significantly rhombic $A_\perp$. The OD terms for Cu_O and Cu_S both slightly increase in the $A_{||}$ direction of the low-

Table 6. Calculated Cu Hyperfine Coupling Constants of the 96-Atom and 97-Atom Models with Program ORCA 2.5 (10^{-4} cm^{-1})

		A(FC)	A(SD)	A(OD)	A(total)^a	
96-atom model	Cu$_S$	−53	−71	72	−52	$A_{\parallel}$
			31	14	−8	$A_{\perp}$
			40	10	−3	
	Cu$_O$	−58	−78	86	−48	$A_{\parallel}$
			31	18	−10	$A_{\perp}$
			47	12	1	
97-atom model	Cu$_S$	−56	−76	91	−48	$A_{\parallel}$
			29	21	−2	$A_{\perp}$
			48	12	4	
	Cu$_O$	−20	−63	91	17	$A_{\parallel}$
			−1	27	−4	$A_{\perp}$
			64	4	49	

^{a} A_{total} is the eigenvalue of three contributions, which is collinear with the **g** tensor in the 96-atom model but is noncollinear in the 97-atom model.

pH form. The total calculated $A_{\parallel}$ values reproduce the experimental results reasonably well; however, the calculated results for $A_{\perp}$ are less satisfactory.

The EPR hyperfine coupling calculations are consistent with the experimental results for the high-pH form, indicating that the two coppers equivalently contribute to the observed seven-line hyperfine coupling in the $g_{\parallel}$ range. Upon going to the low-pH form, the calculated total parallel hyperfine for Cu$_S$ remains at the same; however, the calculated $A_{\parallel}$ is significantly decreased in Cu$_O$. Therefore, the hyperfine couplings for two Cu's are no longer equivalent at low pH, and a four-line pattern in the $g_{\parallel}$ region is expected and observed. As is clear from Table 6, this inequivalence dominantly reflects the difference in the FC term for Cu$_O$ in going from high pH to low pH. This demonstrates that the 1% Cu 4s mixing into the ground state at low pH gives a large contribution to $A_{\parallel}$ as it produces direct positive spin density at the nucleus.

In contrast to the high-pH form, the **A** tensor of the low-pH structure is no longer colinear with the **g** tensor. The possible contribution of this effect on the EPR spectrum of the low-pH form was evaluated through spectral simulations (Figure S6 in Supporting Information). This **A** tensor rotation reduces the hyperfine couplings of both Cu's but does not change the four-line hyperfine coupling pattern. Thus, the colinear simulations of experimental spectra of the low-pH form and the H120A mutant can reasonably reproduce the hyperfine pattern with only minor deviations in the intensity (Figure 1).

C. Excited States. The bonding description developed for Cu$_A$ is given in Figure 7. Each Cu has 5d orbitals, which split in D_{2h} dimer symmetry into 10 levels due to the direct bonding interactions between Cu's and with the bridging S ligands. In addition, each thiolate has two valence 3p orbitals perpendicular to the S−C bond, which contribute to form molecular orbitals for electron delocalization in the Cu$_2$S$_2$ plane. With 19d electrons present in the Cu$^{1.5+}$−Cu$^{1.5+}$ core, a half-occupied ψ^* (RAMO) is formed, which is the σ_u^* (i.e., the Cu−Cu antibonding orbital) ground state. From Figure 7, a series of five parity-allowed (g → u) metal d-orbital-based electronic transitions are predicted for the mixed valence dimer, each involving the promotion of an electron from a doubly occupied orbital to the half-occupied RAMO. In particular, the $\sigma_g \rightarrow \sigma_u^*$ ($a_g \rightarrow b_{3u}$) is the $\psi \rightarrow \psi^*$ transition (band 2 in Figure 2). Alternatively, the four d-orbital-based u → u transitions are parity-forbidden. However, the energy of π_u (b$_{2u}$) has been estimated earlier from the EPR $g_{\parallel}$ value[19,32,33] of Cu$_A$ and will be evaluated below from the MCD C-term associated with the $\psi \rightarrow \psi^*$ transition. The sulfur-based

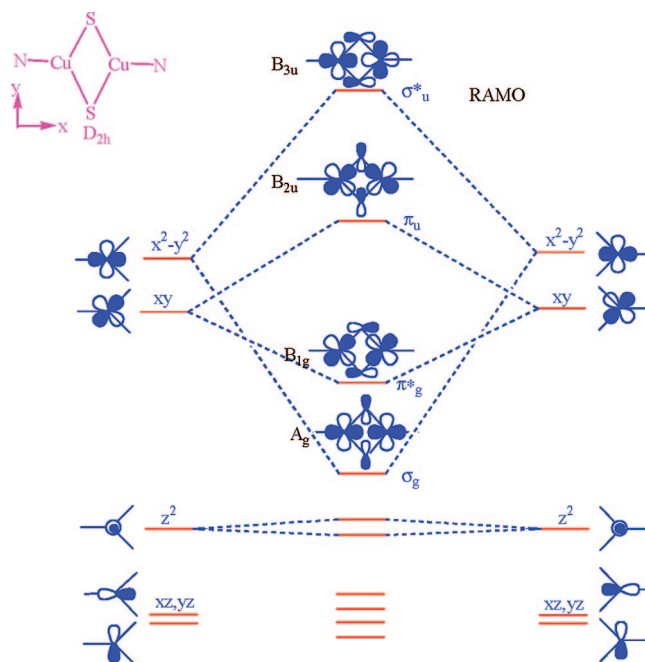**Figure 7.** Simplified molecular orbital diagram of the in-plane Cu$_2$S$_2$ core in Cu$_A$ site demostrates the coupling between two C_{2v} NCuS$_2$ monomers each with its 3d$_{x^2-y^2}$ orbital highest in energy, the 3d$_{xy}$ orbital second, followed by the 3d$_{z^2}$, 3d$_{xz}$, and 3d$_{yz}$ orbitals.
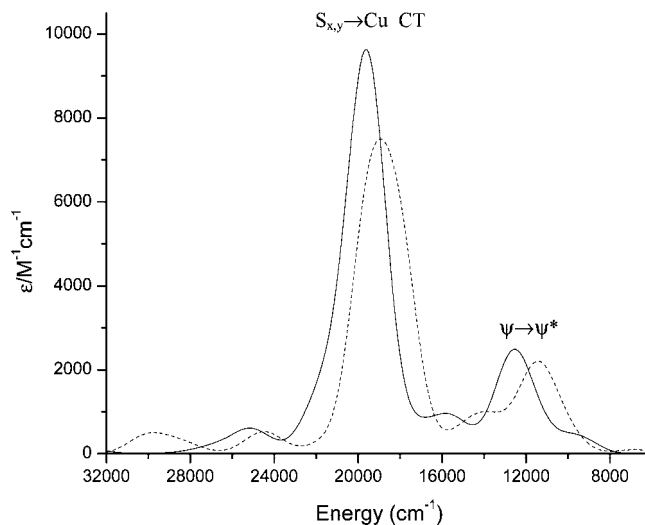

Figure 8. TD-DFT calculated absorption spectra of the high-pH form model (solid line) and the low-pH form model (dashed line).

dimer orbitals give two parity-allowed transitions (S$_{cys} \rightarrow$ Cu CT) involving the sp orbitals in the xy plane.[18,19,56] These correspond to bands 6 and 7 in Figure 2. The pH perturbations on these excited states (in particular, the π_u state) and their effects on the spectroscopy are evaluated below.

(i) TD-DFT. Calculations were applied to simulate the absorption spectrum of the high-pH Cu$_A$ and evaluate the effects of H120 protonation on this spectrum. In Figure 8, the calculated spectrum of the high-pH model reproduces well the experimental absorption spectrum. TD-DFT calculation of the low-pH model shows no dramatic difference, with all peaks red-shifted by ~1000 cm^{-1}. The red shift in the low-energy region of the low-

(56) Neese, F.; Solomon, E. I. *Inorg. Chem.* **1999**, *38*, 1847–1865.

pH form is consistent with experiment, while the red shift in the CT region is not observed in experiment.

The experimental (Figure 2) and computational (Figure 8) decrease of ~ 1000 cm^{-1} in the $\psi \rightarrow \psi^*$ transition energy between the high- and low-pH forms reflects a $\sim 10\%$ decrease in $2H_{AB}$. Interestingly, the Cu–Cu bond distance decreases by 0.04 Å, the Raman shift ν_1 increases by 10 cm^{-1}, and the spin density distribution over Cu$_2$S$_2$ exhibits only a minor change. Thus, a stronger direct Cu–Cu interaction is indicated, which is consistent with a calculated small increase in the Mayer bond order[57] (from 0.37 to 0.39). However, the DFT-optimized structure of the low-pH form indicates a less symmetric Cu$_2$S$_2$ core with the Cu–S distance difference of up to 0.1 Å, a longer S–S distance (increased by 0.06 Å). This decreases the superexchange coupling contribution to $2H_{AB}$. Thus, the relatively limited experimental decrease in $2H_{AB}$ reflects the net effects of opposite contributions of an increased direct Cu–Cu coupling and decreased superexchange contribution through the thiolate bridges.

The TD-DFT calculations predict that the low-lying π_u (b$_{2u}$) state is 4000 cm^{-1} above the σ_u^* (b$_{3u}$) ground state in the high-pH model and 2800 cm^{-1} above the σ_u^* ground state in the low-pH model. This π_u state spin–orbit (S.O.) couples into the σ_u^* ground state and leads to the deviation of the EPR $g_\parallel$ from 2.0023. This is given by:

$$g_\parallel \approx g_e + 8\zeta_{3d}^{Cu}\alpha^2\beta^2/\Delta_{\sigma_u^*/\pi_u} \quad (1)$$

where α^2 is the total Cu character in the σ_u^* ground state, β^2 is the total Cu character in the π_u excited state, $\Delta_{\sigma_u^*/\pi_u}$ is the energy splitting between σ_u^* and π_u, and ζ_{3d}^{Cu} is the Cu 3d S.O. coupling constant. From the DFT calculations, $\Delta_{\sigma_u^*/\pi_u}$ deceases by 1200 cm^{-1} in the low-pH form while the Cu characters of the σ_u^* and π_u states are similar to those in the high-pH form. Thus, the $g_\parallel$ value increases. This is consistent with the experiment: $g_\parallel = 2.173$ for the high-pH form, and $g_\parallel = 2.222$ for the low-pH form. Our previous study gave an experimental estimate for $\Delta_{\sigma_u^*/\pi_u}$ of 5000 cm^{-1} in the high-pH form. From eq 1 and the experimental $g_\parallel$ value, a value of $\Delta_{\sigma_u^*/\pi_u} = 3900$ cm^{-1} is obtained for the low-pH form, which is in qualitative agreement with the TD-DFT calculations.

(ii) The $\psi \rightarrow \psi^*$ MCD C-Term. As given by simplified eq 2, MCD C-term intensity requires two perpendicular nonzero electronic dipole transition moments (M_i) that are also perpendicular to the Zeeman direction.

$$\Delta\epsilon \propto g_z M_x M_y + g_x M_y M_z + g_y M_z M_x \quad (2)$$

In the $<D_{2h}$ symmetry of the Cu$_A$ site, all states are nondegenerate, thus all the electronic transitions are unidirectional. Therefore, MCD intensity requires the S.O. coupling between states with perpendicular transition moments. From Figure 2, the LT MCD spectra of Cu$_A$ sites show two types of behavior: a derivative shaped, pseudo-A term[58] in the S$_{cys} \rightarrow$ Cu CT region (bands 6 and 7) and a negative C-term feature in the $\psi \rightarrow \psi^*$ transition region (band 2). The mechanism of the pseudo-A term in the CT region has been evaluated.[18,19,56] The nonzero C-term intensity can be obtained by S.O. coupling between two nearby excited states, to which the orthogonal transitions are made from the ground state σ_u^*. The two nearby excited states in the Cu$_A$

(57) Mayer, I. *Chem. Phys. Lett.* **1983**, *97*, 270.
(58) The derivative shape leads to an A-term description, but the temperature dependence of this signal shows that it is a combination of equal but opposite C-terms.
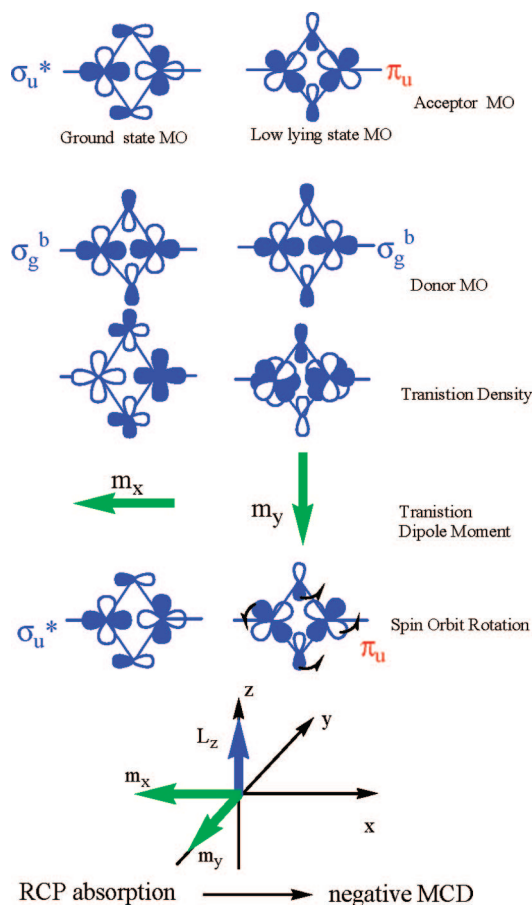
Figure 9. Graphic prediction of the C-term sign for the $\psi \rightarrow \psi^*$ transition (i.e., $\sigma_g^b \rightarrow \sigma_u^*$).

site correspond to the two thiolate ligand-based CT states which are allowed and polarized in the Cu$_2$S$_2$ plane (i.e., the xy plane, x is along the Cu–Cu vector). They S.O. couple in the z direction. This produces the equal and opposite signed MCD features (the temperature-dependent pseudo-A term).

Alternatively, an isolated C-term feature would be obtained if there is a low-lying (nonthermally accessible) state with a transition to the same excited state polarized perpendicular to the transition from the ground state σ_u^* that can S.O. couple in a third perpendicular direction. From the EPR and TD-DFT results, the π_u state is energetically near the σ_u^* ground state ($\Delta_{\pi_u/\sigma_u^*} = 5000$ cm^{-1} for the high-pH form). This state can S.O. couple into the σ_u^* ground state in the z direction. The $\psi \rightarrow \psi^*$ transition (i.e., $\sigma_g \rightarrow \sigma_u^*$) is x polarized, and the $\sigma_g \rightarrow \pi_u$ transition is y polarized as shown in Figure 9. The MCD signal for the $\psi \rightarrow \psi^*$ transition is predicted to be negative. This is consistent with the negative C-term for the $\psi \rightarrow \psi^*$ transition of Cu$_A$.

In going from high pH to low pH, from both the TD-DFT calculations and EPR $g_\parallel$ values, the $\Delta_{\pi_u/\sigma_u^*}$ energy is decreased by ~ 1000 cm^{-1}. Thus, a more intense MCD signal of the $\psi \rightarrow \psi^*$ transition is expected in the low-pH form. Our experimental data show that the ratios of the MCD C-term intensity to the absorption intensity of band 2, the C_0/D_0 values, are 0.43 ± 0.06 in the high-pH form and 0.55 ± 0.10 in the low-pH form. The difference between these is within the error bar, and the expected increase in the C_0/D_0 value cannot be unambiguously resolved due to the overlap of bands 2 and 3 in both the high- and low-pH forms. However, compared with the C_0/D_0 values

of the d $\rightarrow$ d transitions of monomer Cu centers (i.e., a localized Cu site), which are $\sim$0.1,[59] the large C_0/D_0 value of band 2 in Cu$_A$ ($\sim$0.5) strongly supports the valence delocalized descriptions for both the high- and low-pH forms. The large C_0/D_0 value reflects the presence of the low-lying π_u state that effectively S.O. couples into the ground state. In monomers and localized mixed valence systems, the d$-$d excited state energies are much higher, leading to less effective S.O. coupling into the ground state. This lowers the C_0/D_0 contribution from S.O. mixing into the ground state, thus in localized systems, the MCD C-term intensity mostly reflects S.O. coupling between ligand field excited states (i.e., pseudo-A terms).

Discussion

A. Spectral Probes of Delocalization. Apparent localization is observed from the EPR spectra of Cu$_A$ at low pH and in its H120A mutant. However, the rR and MCD C-term data provide clear evidence for valence delocalization. This is consistent with the Q-band ENDOR results on the H120A mutant where the nitrogen ligand of the unperturbed histidine (His46) exhibits a very similar hyperfine coupling to that of the delocalized Cu$_A$ site.[38]

For the high-pH and the low-pH/H120A models, the DFT calculations reveal a delocalized σ_u* ground state with a similar spin density distribution over the Cu$_2$S$_2$N$_{His46}$ core. In the high-pH form, each Cu has a relatively small negative contribution to the hyperfine coupling due to the delocalization of the electron spin over d$_{x^2-y^2}$ orbitals on the two Cu centers. In the low-pH form, the $\sim$1% 4s mixing due to the distorted ligand field of Cu$_A$ adds a direct Fermi contact contribution to the hyperfine coupling, which is large and positive. The net effect is to generate a smaller Cu$_O$ hyperfine coupling to the electron spin, even though it has about as much total spin density as the nonperturbed Cu$_S$ center. Thus the EPR spectrum can be misleading with respect to delocalization, due to the potentially large effects of small contributions to the ground-state wave function.

B. Factors Effecting Delocalization. The electron delocalization of the high-pH form of Cu$_A$ has been evaluated in terms of the Q$_-$ mode in PKS model[19,60,61] (eq 3).

$$E^{\pm} = \frac{1}{2}\left(\frac{\Lambda^2}{k_-}\right)x^2 \pm \left[\frac{1}{2}\left(\frac{\Lambda^2}{k_-}x_- + \frac{\Delta E}{\sqrt{2}}\right)^2 + H_{AB}^2\right] \quad (3)$$

The dimensionless coordinate x_- is along the Q$_-$ mode (Q$_-$ is the antisymmetric combination of the breathing modes of the two Cu centers), Λ^2/k_- is the vibronic trapping term associated with the change in the Cu$-$L bond lengths upon oxidation, ΔE is the potential difference between monomers, and H_{AB} is the electronic coupling matrix element regulating electron delocalization between Cu's. In the high-pH form of Cu$_A$, the two coppers have approximately equivalent ligand field ($\Delta E \sim 0$) and the large $2H_{AB}$ (13 300 cm^{-1}) overcomes the vibronic
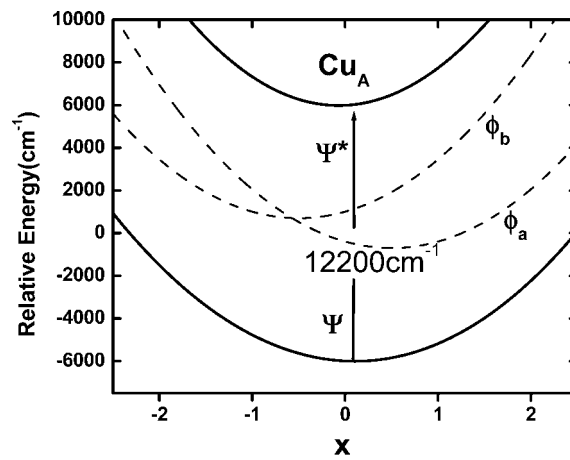
(59) Solomon, E. I.; Szilagyi, R. K.; George, S. D.; Basumallick, L. *Chem. Rev.* **2004**, *104*, 419–458.

(60) With the monomeric breathing modes QA and QB, the Q$_-$ mode is $2^{-1/2}$(QA$-$QB). The dimensionless coordinate x_- is along the Q$_-$ mode, $x_- =$ Q$_-/(\Lambda/k_-)$, where $k_- = 4\pi^2c^2\mu_-\nu_-^2$ in which ν_- and μ_- are the frequency and modal mass of the Q$_-$ mode, respectively. The quantity Λ is the vibronic coupling parameter where $\Lambda 2/k_- \approx k_-[n^{1/2}\Delta r_{redox}]^2$, in which n is the number of metal$-$ligand bond length changes and Δr_{redox} is the difference in metal$-$ligand bond lengths between the oxidized and reduced structures.

(61) Piepho, S. B.; Krausz, E. R.; Schatz, P. N. *J. Am. Chem. Soc.* **1978**, *100*, 2996–3005.

Figure 10. Potential energy surfaces in Q$_-$ mode for the low-pH form of Cu$_A$ site. The specific parameters used are $2H_{AB}$ =12 000 cm^{-1}, Λ^2/k_- = 2450 cm^{-1}, ΔE = 0.120 eV.

trapping and keeps the Cu$_A$ center delocalized even in the low symmetry protein environment. Thus, the two Cu's of the high-pH form have equivalent contributions to the ground-state wavefuction (i.e., complete delocalization).

In the low-pH form, one histidine is protonated, and the two Cu's are no longer equivalent. From DFT calculations with either Cu$_O$ or Cu$_S$ replaced by Zn^{2+}, we estimate an energy difference of $\Delta E \sim 0.120$ eV favoring the Cu$_O$ oxidation in the low-pH geometry. The electronic coupling term $2H_{AB}$ in the low-pH form decreases by $\sim$10%, which reflects the decrease in the superexchange contribution (vide supra). Using this experimental $2H_{AB}$ and the calculated ΔE, regression analysis of eq 3 gives the relative contribution of Cu$_O$/Cu$_S$ = 58:42 to the ground-state wave function. The ground- and excited-state potential energy surfaces of the low-pH form are plotted in Figure 10. The two dashed lines indicate the potential energy surfaces of valence-trapped Cu$_A$. Only one minimum is observed in the ground-state potential energy surface, indicating that the low-pH form is still a delocalized system and the $2H_{AB}$ ($\sim$12 000 cm^{-1}) is large enough to overcome vibronic trapping even with the inequivalent potentials of the two Cu centers.

C. Correlation of Electronic Structure to ET and Its Regulation by [H$^+$]. The valence delocalized electronic structure of Cu$_A$ contributes to its efficiency in biological ET. According to semiclassical Marcus theory, the rate of long-range ET[62–64] is dependent upon the following factors: λ, H_{DA}, and $\Delta G°$, where λ is the reorganization energy associated with the active site geometry change with redox, H_{DA} is the through protein electronic coupling between the donor and acceptor, and $\Delta G°$ is the thermodynamic driving force. The rate of electron transfer is enhanced by maximizing H_{DA} while minimizing the sum of $\lambda + \Delta G°$. Here we consider how these factors change in going to the low-pH form.

(i) Reorganization Energy. The high-pH form of Cu$_A$ has a reorganization energy of $\sim$0.4 eV,[65,66] which is $\sim$½ that of the monomer (i.e., localized) blue copper site ($\sim$0.80 eV).[59] This

(62) Beratan, J. N.; Betts, J. N.; Onuchic, J. N. *Science* **1991**, *252*, 1285–1288.

(63) Marcus, R. A.; Sutin, N. *Biochim. Biophys. Acta* **1985**, *811*, 265–322.

(64) Newton, M. D. *Chem. Rev.* **1991**, *91*, 767–792.

(65) Brezezinski, P. *Biochemistry* **1996**, *35*, 5611–5615.

(66) Farver, O.; Lu, Y.; Ang, M. C.; Pecht, I. *Proc. Natl. Acad. Sci. U.S.A.* **1999**, *96*, 899–902.
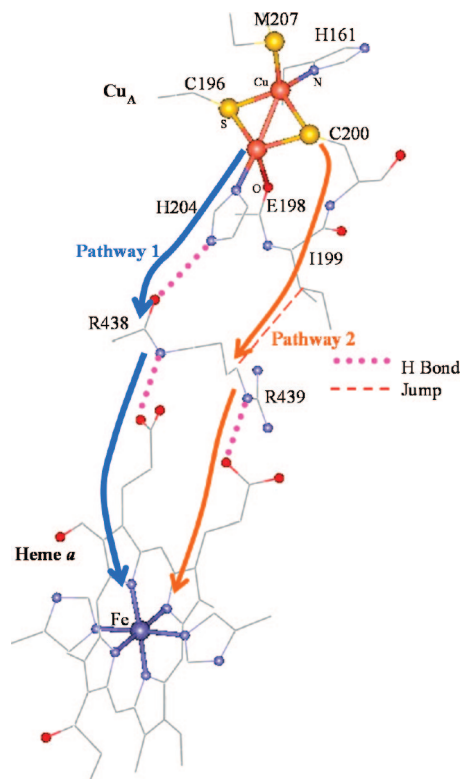
Figure 11. Proposed ET pathways in bovine heart C*c*O based on pathways analysis (ref 34). The Cys200 and His204 Cu$_A$-to-heme *a* pathways are comparable in rate.

low reorganization energy for Cu$_A$ results from the delocalized nature of the ground state which distributes redox-induced geometric changes over the 2Cu's.[19,67] In going to the low-pH form, the reorganization energy increases by 0.18 eV, as determined by Pecht and co-workers.[68] Consistent with the experimental results, the calculated inner sphere reorganization energies are 0.36 eV for the high-pH model and 0.50 eV for the low-pH model. Pecht and co-workers attributed this increase to localization in the low-pH form. However, from the above spectroscopic results, the low-pH form is delocalized. In the low-pH form, there is a H$_2$O ligand on Cu$_O$, which will be lost on reduction. In the mononuclear (i.e., localized) red copper site, there is also a H$_2$O ligand which is lost upon reduction. The reorganization energy of red copper is 1.2 eV.[69] Thus, even in the low-pH form of Cu$_A$, the delocalization over 2Cu's significantly decreases the effect on λ associated with the loss of a H$_2$O ligand upon reduction.

(ii) Superexchange Pathways. Two efficient intramolecular ET pathways from Cu$_A$ to heme *a* have been recognized[34] (Figure 11). Pathway 1 (His204 to heme *a*) has a calculated ET rate similar to the experimental rate (1×10^4 s^{-1}). The calculated ET rate of pathway 2 (Cys200 to heme *a*) is 2 orders of magnitude less efficient than pathway 1 (8.0×10^1 s^{-1}). However, correcting this for the anisotropic covalency of the Cu–S$_{cys}$ bond of pathway 2 relative to the Cu–N$_{his}$ bond of pathway 1, pathway 2 becomes comparable to pathway 1.[34]

Table 7. Cu$_A$ to Heme *a* ET Rate Comparison between the High- and Low-pH Forms of Cu$_A$

	Cu$_A$ → heme *a*	
	high pH	low pH
λ (eV)	0.40	0.49
ΔG (eV)[a]	−0.05	0.03
$k_{ET}^{high\,pH} / k_{ET}^{low\,pH}$ (calcd)[b]	11[c]	
experiment k_{ET} s^{-1} [a]	90000	45
$k_{ET}^{high\,pH} / k_{ET}^{low\,pH}$ (exptl)	2000	

[a] Experimental results are from kinetic analyses of ET rate of the R.s. C*c*O and its H260N mutant. The Cu$_A$ site in H260N mutant corresponds to the low-pH form in this table. The reduction potential of the Cu$_A$ site in H260N mutant increases by ∼90 mV (ref 68) (the reduction potential of the low-pH form of Cu$_A$ azurin increases by ∼70 mV). [b] $k_{ET} = \sqrt{\pi / \hbar^2 \lambda k_B T} \cdot (H_{DA})^2 \cdot \exp\left[- (\Delta G^o + \lambda)^2 / 4\lambda k_B T \right]$. [c] Assuming the same donor–acceptor coupling strength $(H_{DA})^2$ for both pH forms.

The H120 ligand in Cu$_A$ azurin corresponds to H204 in bovine heart C*c*O, which is along ET pathway 1 (Figure 11). There are three direct effects in the ET rate due to the H204 protonation at low pH: the loss of the pathway 1 in Cu$_A$ → heme *a* ET, an increase in λ, and an increase in the Cu$_A$ reduction potential by ∼70 mV.[37] Considering the second and third factors and assuming the same donor–acceptor coupling strength H^2_{DA} in ET for both pH forms, the ET efficiency of the low-pH form is predicted to be ∼11-fold slower than that of the high-pH form. Experimentally (in the related R.s. C*c*O, and its H260N mutant[70]), this ratio is much larger (2000-fold in Table 7). This ∼180-fold difference cannot result from the loss of one of two comparable pathways which can only give ∼2-fold decrease. However, pathway 2 involves a 1.86 Å through space jump from an Ile to an Arg residue. The Ile is next to the Glu that is axially coordinated to Cu$_O$. In the calculated geometric structure of the low pH/His mutant model, the distance of Cu$_O$ to O$_{glu}$ ligand decreases by 0.26 Å with respect to the high-pH model. This elongates the space between the Ile and Arg residues. In addition, based on the crystal structure (PDB: 1V54), the imidazole ring of H204 in C*c*O is near the Ile residue, and its protonation can shift the Ile residue further away from the Arg residue. The calculated through space jump decays rapidly ($H^2_{DA} \propto (0.6 e^{-1.7(R-1.4)})^2$, where R is the through space distance);[62,71] H^2_{DA} can decrease by ∼30-fold if the through space distance is increased by ∼1.0 Å. Combined, these factors would contribute to a ∼660-fold decrease in the ET rate in the low-pH form.

(iii) Possible Contribution to Function. While the identification of the exit pathway for pumped protons is still lacking, the direct role of Cu$_A$ in proton pumping lost support with the discovery of the heme–Cu oxidase of *Escherichia coli*, cytochrome *bo$_3$* which pumps protons but does not contain Cu$_A$.[72,73] However, the reversible pH effect on Cu$_A$ studied above could play a role in PCET through regulating ET upon local proton accumulation.

Summary

This study provides a detailed understanding of the pH effect on the geometric and electronic structure of the Cu$_A$ site. In

(67) Larrson, S.; Källebring, B.; Wittung, P.; Malmström, B. G. *Proc. Natl. Acad. Sci. U.S.A.* **1995**, *92*, 7167.
(68) Farver, O.; Hwang, H. J.; Lu, Y.; Pecht, I. *J. Phys. Chem. B* **2007**, *111*, 6690–6694.
(69) Basumallick, L.; Sarangi, R.; George, S. D.; Elmore, B.; Hooper, A. B.; Hedman, B.; Hodgson, K. O.; Solomon, E. I. *J. Am. Chem. Soc.* **2005**, *127*, 3531–3544.

(70) Wang, K.; Geren, L.; Zhen, Y.; Ma, L.; Ferguson-Miller, S.; Durham, B.; Millett, F. *Biochemistry* **2002**, *41*, 2298–2304.
(71) Beratan, D. N.; Onuchic, J. N.; Betts, J. N.; Bowler, B. E.; Gray, H. B. *J. Am. Chem. Soc.* **1990**, *112*, 7915–7921.
(72) Puustinen, A.; Finel, M.; Virkki, M.; Wikström, M. *FEBS Lett.* **1989**, *249*, 163–167.
(73) Hosler, J. P.; Ferguson-Miller, S.; Mills, D. A. *Annu. Rev. Biochem.* **2006**, *75*, 165–187.

particular, EXAFS studies show that the bond distances in the Cu$_2$S$_2$ core of the high-pH and low-pH forms of Cu$_A$ and its H120A mutant are very similar, and the rR and MCD spectra demonstrate electron delocalization. This is due to the large $2H_{AB}$ and dominantly reflects a strong direct Cu−Cu interaction that keeps the Cu$_A$ site delocalized in the low-symmetry protein environment, even with the protonation and loss of a His liagnd. DFT calculations support this electron delocalization description and provide insight into the change in spectral features with pH. Importantly, the four-line EPR hyperfine coupling pattern in the low-pH form is not due to electron localization but rather reflects ~1% Cu$_O$ 4s mixing into the ground-state spin wave function. This reversible pH effect can play an important role in regulating ET under in vivo conditions.

Supporting Information Available: Complete ref 44; fits to absorption, MCD, and CD spectra, the rR excitation profiles of the high-pH and low-pH forms, fits to EXAFS data, and XSophe simulations of the effect of the **A** tensor ratio on the EPR hyperfine coupling pattern are available. This material is available free of charge via the Internet at http://pubs.acs.org.

JA7102668